

# Beyond Early Development: Observing Zebrafish over 6 Weeks with Hybrid Optical and Optoacoustic Imaging

Paul Vetschera, Benno Koberstein-Schwarz, Tobias Schmitt-Manderbach, Christian Dietrich, Wibke Hellmich, Andrei Chekkoury, Panagiotis Symvoulidis, Josefine Reber, Gil Westmeyer, Hernán López-Schier, Murad Omar, and Vasilis Ntziachristos\*

Zebrafish are common model organisms in developmental biology, but have recently emerged as imaging targets of research in cancer, tissue regeneration, metabolic disorders, functional genomics, and phenotype-based drug discovery. Conventionally, zebrafish are studied during the first few days of development using optical microscopy methods. However, optical methods are not suited for imaging at later stages, since the fish become opaque. To address needs to visualize beyond the first days of development, a novel multimodality system for observing zebrafish from larval stage to adulthood is developed. Using a hybrid platform for concurrent selective plane illumination microscopy (SPIM) and optoacoustic mesoscopy, fish (ex vivo) at stages of development up to 47 days at a similar object size-to-resolution ratio are imaged. Using multiple wavelength illumination over the visible and short-wavelength infrared regions, it is demonstrated that the optoacoustic method can follow GFP-based contrast used in SPIM, enabling molecular imaging interrogation in adult fish. Moreover, the optoacoustic modality reveals zebrafish features based on optical contrast absent in SPIM, including contrast from endogenous blood, water, and lipids. It is discussed how the hybrid system method can enable the study of zebrafish in a wider range of applications and over time-scales not possible currently when using optical microscopy.

## 1. Introduction

Zebrafish (*Danio rerio*) are widely used in developmental biology as they are transparent during the early stages of development and therefore can be visualized by optical microscopy. Employed as a model organism, zebrafish are attractive for laboratory studies as they are easy to breed to large numbers and can be genetically manipulated to explore functional genomics and diverse cellular processes. Therefore, zebrafish are now increasingly considered in a wider number of applications, including modeling biological processes in cancer, tissue regeneration, or metabolic disorders<sup>[1,2]</sup> or to support the development of personalized anticancer treatment by serving to grow patient-derived xenografts with much less patient material than when using mice.<sup>[3]</sup> Zebrafish have been also used in drug screening,<sup>[4]</sup> in toxicity studies for drugs or environmental contaminants and to screen neuroactive compounds for their ability to modify behavior.<sup>[5]</sup>

P. Vetschera, B. Koberstein-Schwarz, A. Chekkoury, P. Symvoulidis<sup>[+]</sup>, J. Reber, G. Westmeyer, M. Omar, V. Ntziachristos  
Institute of Biological and Medical Imaging (IBMI)  
Helmholtz Zentrum München  
85764 Neuherberg, Germany  
E-mail: bioimaging.translatum@tum.de

P. Vetschera, B. Koberstein-Schwarz, A. Chekkoury, P. Symvoulidis<sup>[+]</sup>, J. Reber, M. Omar, V. Ntziachristos  
Chair of Biological Imaging at the Central Institute for Translational Cancer Research (TranslaTUM)  
Technical University Munich  
81675 Munich, Germany

B. Koberstein-Schwarz, T. Schmitt-Manderbach, C. Dietrich, W. Hellmich  
Carl Zeiss AG  
Corporate Research and Technology  
07745 Jena, Germany

P. Symvoulidis<sup>[+]</sup>  
Institute of Developmental Genetics  
Helmholtz Zentrum München  
85764 Neuherberg, Germany

G. Westmeyer, V. Ntziachristos  
Munich Institute of Biomedical Engineering (MIBE)  
Technical University of Munich  
85748 Garching b. München, Germany

G. Westmeyer  
Institute of Synthetic Biomedicine  
Helmholtz Zentrum München  
85764 Neuherberg, Germany

 The ORCID identification number(s) for the author(s) of this article can be found under <https://doi.org/10.1002/lpor.202200846>

[+]Present address: MIT Center for Neurobiological Engineering, Massachusetts Institute of Technology (MIT), Cambridge, Massachusetts 02139, USA

© 2023 The Authors. Laser & Photonics Reviews published by Wiley-VCH GmbH. This is an open access article under the terms of the Creative Commons Attribution License, which permits use, distribution and reproduction in any medium, provided the original work is properly cited.

DOI: 10.1002/lpor.202200846

Despite the wealth of possible applications, *in vivo* studies are limited to the embryonic and early larval stages, i.e., stages when the fish are small (thin) and transparent, so they can be visualized by optical microscopy. However, zebrafish imaging from late larval stages to adulthood is challenging using optical methods due to the appearance of scattering as the fish develops. Therefore, while optical interrogation has provided critical insights in development and disease, it is not well suited for capturing longitudinal processes, such as long-term drug effects or toxicity, age-related functional alterations common in diseases like metabolic disorders,<sup>[5]</sup> or morphogenesis and tissue remodeling functions that continue throughout adulthood.<sup>[6]</sup>

Depending on the particular method and the amount of scattering present, optical microscopy may penetrate to depths of up to 1 mm.<sup>[7]</sup> Since the body thickness of zebrafish ranges from less than 100  $\mu\text{m}$  in the early larval stage to nearly 1 cm in adult specimens, optical microscopy can only be used to visualize whole specimens during the first few weeks of development. Selective plane illumination microscopy (SPIM) has been proposed for imaging specimens up to the late larval stage. By illuminating tissue using a thin sheet of light passing through the specimen, SPIM offers a way to reduce the sensitivity to photobleaching and achieve volumetric imaging of living organisms. The low laser energy used in SPIM together with the fast acquisition speed makes it well suited for *in vivo* imaging. Multiple studies<sup>[8]</sup> have already shown the value of SPIM for imaging small model organisms, such as the *in vivo* SPIM imaging of the beating heart of a 5-day-old zebrafish.<sup>[9]</sup> However, SPIM imaging is not feasible in older, larger zebrafish, since SPIM resolution rapidly degrades due to aberrations when specimens are thicker than 200  $\mu\text{m}$  and SPIM cannot be used for visualization through media with increased scattering. For this reason, larger organisms have to be chemically treated to render them optically clear for SPIM imaging, but such treatment is toxic and does not allow *in vivo* measurements.<sup>[10]</sup> An engineered zebrafish strain called crystal is translucent as an adult and has proven useful in cancer studies,<sup>[11]</sup> but the genetic alterations in this strain are not entirely understood and may interfere with interpretation of results.<sup>[2]</sup>

To enable imaging at later developmental stages, we consider herein the combination of SPIM with optoacoustic imaging in a hybrid microscopy system. Optoacoustic imaging can visualize beyond the penetration depth limits of optical microscopy as it is not sensitive to scattering and therefore appropriate for imaging opaque tissues.<sup>[7]</sup> When implemented with broad tissue illumination, the optoacoustic resolution depends on ultrasound diffraction, i.e., the ultrasound bandwidth detected.<sup>[7,12,13]</sup> By utilizing ultrawide bandwidth detection spanning  $\approx 10$ –200 Mhz, we have already demonstrated the collection of rich information contrast from tissues in the mesoscopic regime at resolutions of a few to tens of micrometers at depths of a few millimeters in tissue.<sup>[12–20]</sup> For example, a 1-week-old zebrafish has been imaged with raster-scan optoacoustic mesoscopy (RSOM)

at a lateral resolution of 18  $\mu\text{m}$  in the 20–180 MHz frequency range,<sup>[15]</sup> while an axial resolution as high as 4  $\mu\text{m}$  has been observed at the higher end of the frequency spectrum. Other optoacoustic implementations have resolved zebrafish at lower frequencies, demonstrating resolutions in the range of several tens of micrometers.<sup>[12,21–24]</sup> One optoacoustic imaging advantage is that multiple excitation wavelengths can be used to image different sources of contrast, such as blood, melanin,<sup>[14,17]</sup> lipids, and water,<sup>[25–27]</sup> yet this multiwavelength feature has rarely been used for imaging small organisms.<sup>[14,17]</sup>

The combination of SPIM and optoacoustics in one hybrid system can allow high imaging scalability, by allowing optical diffraction resolution images when imaging small and thus transparent zebrafish, while enabling ultrasound diffraction images as the fish grows larger and opaque. We implemented the optoacoustic mode as a multiprojection optoacoustic mesoscopy mode, using ultrasound detectors collecting projections over 360° from the rotating sample embedded in an agarose cylinder. The center of the sample rotation was coaligned with the field of view (FOV) of the SPIM system. This tomographic approach is essential for enabling isotropic resolution, which offers advantages over one-sided looking systems such as RSOM.<sup>[15]</sup> One-sided looking systems offer only limited projection viewing through the sample and thus provide limited information on structures that are perpendicular to the detector area. We hypothesized that the hybrid system could provide the capability to carry out longitudinal studies of small organisms over several weeks, allowing us to overcome the fundamental limitations of current SPIM systems. A critical design parameter for the hybrid operation related to the contrast that could be visualized by the two modalities and, in particular, whether reporter proteins, i.e., fluorescent proteins, could be captured by both SPIM and optoacoustic mesoscopy. Additionally we investigated zebrafish features that could be resolved by optoacoustics at different illumination wavelengths, complementing features imaged by SPIM. We show that the use of sensitive ultrasound detection allowed signals from green fluorescent proteins (GFPs) to be longitudinally visualized by both SPIM and optoacoustic mesoscopy from the early stages of development up to 2 months of fish growth, i.e., at completely opaque conditions. Moreover, using different wavelengths at the optoacoustic mode, we observe various features of fish due to contrast provided by blood, water, and lipid. We further show how the integration of the two modalities into a single system, using a novel sample holder designed for hybrid operation, allows optical and optoacoustic images to be precisely coregistered. We discuss how the hybrid method developed can enable the study of zebrafish in a wider pool of applications and enhance the use of this model organism as a tool for biological discovery and clinical translation.

## 2. Results

The hybrid optical and optoacoustic implementation was based on a common imaging chamber housing a SPIM and an optoacoustic mesoscopy system (**Figure 1**). To accommodate both modalities and enable full 360° viewing for optoacoustic mesoscopy, a new SPIM design was introduced that enables multiorientation scanning and illumination over the entire visible range from 420 to 700 nm. To integrate optoacoustic mesoscopy into the system, a beam with a homogeneous profile of

---

H. López-Schier  
Research Unit Sensory Biology and Organogenesis  
Helmholtz Zentrum München  
85764 Neuherberg, Germany

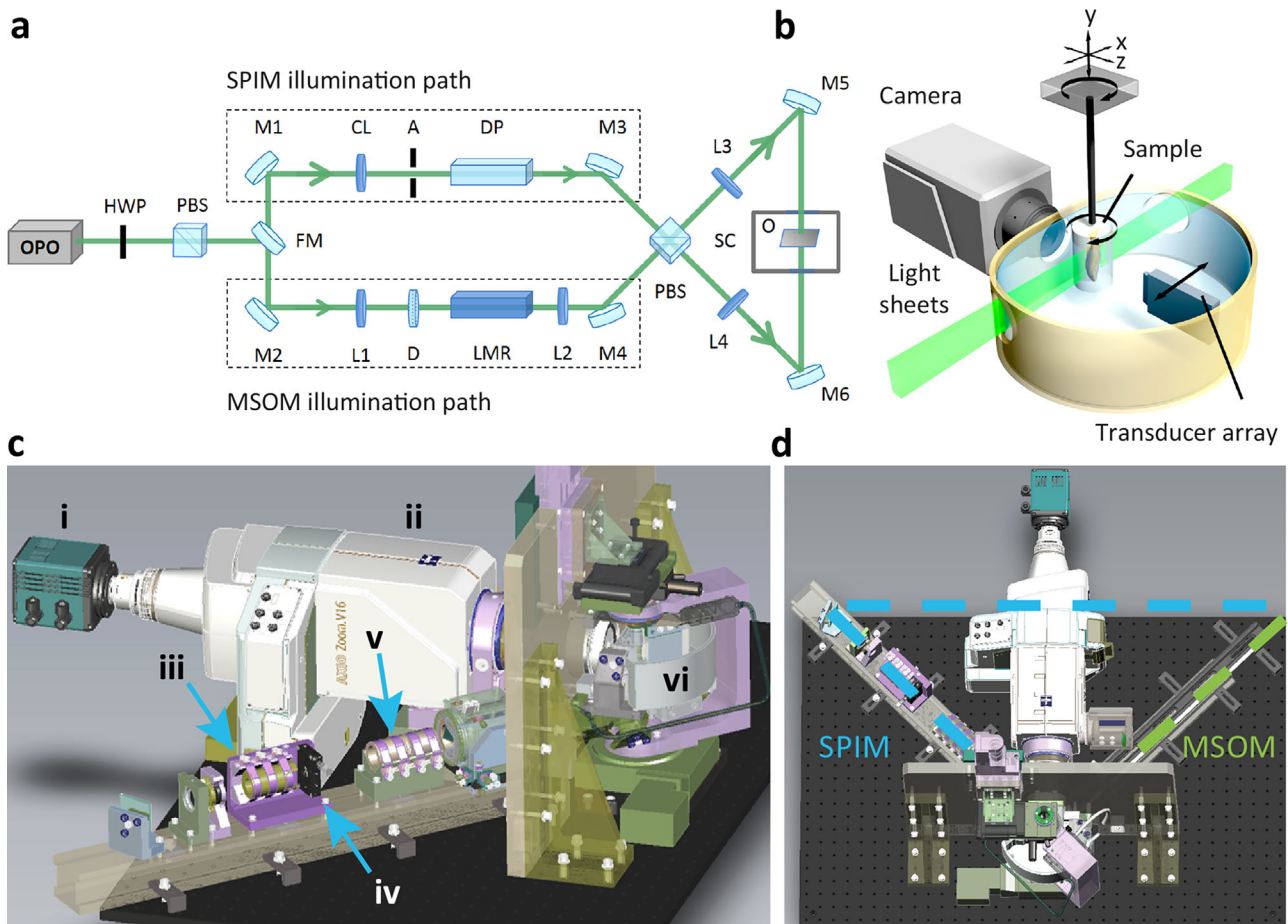


**Figure 1.** Schematic of the SPIM-optoacoustic mesoscopy set-up. a) A pulsed optical parametric oscillator (OPO) laser illuminates first a half-wave plate (HWP) and a polarizing beam splitter (PBS) for power control and then a flip mirror (FM), which is used to choose between light sheet illumination for SPIM or broadfield illumination for optoacoustic imaging. The light sheet illumination involves a cylindrical lens (CL), aperture (A) and dove prism (DP); volumetric illumination for optoacoustic mesoscopy involves a lens (L1), diffusor (D) and light mixing rod (LMR). The pulse energy is adjusted using a motorized HWP and a PBS; beam size is optimized using lenses L2-L4. A second PBS splits the beam 50:50 before illuminating the object (O) in the sample chamber (SC). Plane mirrors (M1-6) are used to redirect the light in the set-up. b) Enlarged view of the sample chamber. The sample is placed in an agar block, which is rotated around the indicated axis to provide multiple views and to allow optoacoustic tomography. In SPIM mode, the sample is linearly translated through the light sheets and subsequently rotated by  $90^\circ$  for multiple views. During optoacoustic acquisition, the sample is rotated  $360^\circ$  and the transducer array is linearly translated in the  $x$ -direction at each angle position. c) CAD-generated side view of the hybrid system, showing the camera (i), optical zoom (ii), cylindrical lens (iii), aperture (iv), diaphragm prism (v), and sample chamber (vi). d) CAD-generated top view of the hybrid system. The dashed lines show the two beam paths for SPIM (blue) and optoacoustic mesoscopy (green).

$10 \times 10 \text{ mm}^2$  was created in a second illumination path by using a diffusor and light-mixing rod. The sample is homogeneously illuminated from two sides and rotated over a full angle range of  $360^\circ$  during optoacoustic mesoscopy acquisition, while the linear transducer array is translated over the entire field of view at each angle position. The central frequency of the linear array was chosen to be 24 MHz to provide suitable resolution and penetration depth for imaging of morphogenesis of model organisms such as zebrafish. The cylindrically-focused 128 elements detect ultrasound signals from a distance of  $\approx 8 \text{ mm}$  from the sample center. As a result, the optoacoustic mesoscopy modality enables volumetric imaging with a FOV of  $10 \times 10 \times 10 \text{ mm}$ . An optical parametric oscillator (OPO) laser with a broad spectral range (420–2300 nm) is used to deliver nanosecond pulses, which stimulate acoustic emission from several absorbing tissue compounds, such as melanin, hemoglobin, water, and lipid. During sample

analysis with this hybrid system, typically SPIM images are first acquired, followed by optoacoustic mesoscopy scanning. Acoustic signals are volumetrically reconstructed using a filtered back-projection algorithm. Finally, SPIM and optoacoustic mesoscopy images can be co-registered based on the positions of the translation and rotation stages during data acquisition.

First, we characterized the performance of the hybrid system using agar phantoms containing fluorescent and polystyrene beads in the  $x$ ,  $y$ , and  $z$ -directions using a common coordinate system for the SPIM and the optoacoustic modalities (Figure 1b). Figure 2a,b shows SPIM images of a  $10 \mu\text{m}$  fluorescent bead, indicating resolution of  $\approx 35 \mu\text{m}$  along the  $z$  axis and  $10 \mu\text{m}$  along the  $x$  and  $y$  axis (Figure 2e). The lateral resolution in the  $x$ - and  $y$ -directions is restricted by the optical zoom and the camera. For the largest possible FOV with the optical zoom, a theoretical lateral resolution of  $6.15 \mu\text{m}$  can be achieved. Figure 2c,d shows

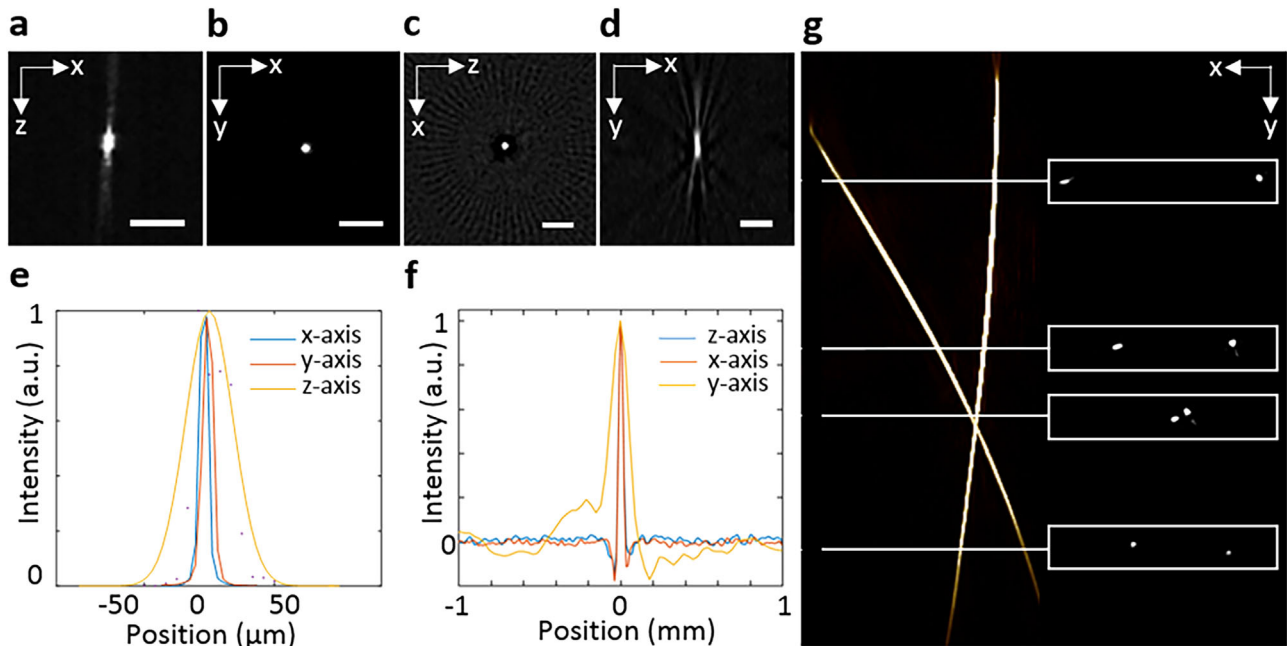


**Figure 2.** Characterization of the SPIM-optoacoustic mesoscopy hybrid system. a,b) A 10 μm fluorescent bead recorded with SPIM in top and side view. c,d) A 20 μm polystyrene bead from two different perspectives as acquired with optoacoustic mesoscopy after reconstruction. e) Profile plot for the 10 μm fluorescent bead measured with SPIM. f) Profile plot for the 20 μm polystyrene bead in the  $x$ ,  $y$ , and  $z$ -directions as measured with optoacoustic mesoscopy. The resolution of the optoacoustic mesoscopy modality was determined to be  $35 \times 35 \times 120 \mu\text{m}$  based on full width at half-maximum in the profiles. g) Full-view image of crossed 20 μm sutures acquired with the optoacoustic mesoscopy modality. The boxed insets show the cross-section from the top.

optoacoustic mesoscopy images of a 20 μm polystyrene bead, indicating a resolution of 35 μm along the  $x$  and  $y$  axes, and 120 μm along the  $z$  axis (Figure 2f). Figure 2g shows images of crossed sutures with a diameter of 20 μm, demonstrating the location-independent high resolution over the full FOV.

Next, we used the SPIM-optoacoustic mesoscopy system to image Tg(pou4f3:GAP-GFP) transgenic zebrafish (*Danio rerio*) expressing GFP in hair cells and optic nerves from early development to adulthood. The morphogenetic development of Tg(pou4f3:GAP-GFP) from transparent to opaque and its strong GFP expression make it an ideal candidate for demonstrating the potential of the hybrid SPIM-optoacoustic system. For these imaging studies, we used a single excitation wavelength of 488 nm for both modalities. This wavelength allowed us to capture GFP fluorescence using SPIM as well as contrast from melanin and blood using optoacoustic mesoscopy. To compare the two modalities at different depths, we measured the variance in sharpness, since scattering of light “blurs” SPIM images of deeper structures and reduces image sharpness. The variance was calculated for a region of interest (corresponding to a support window  $\Omega$ ) and gray value intensity  $u(x, y)$ .

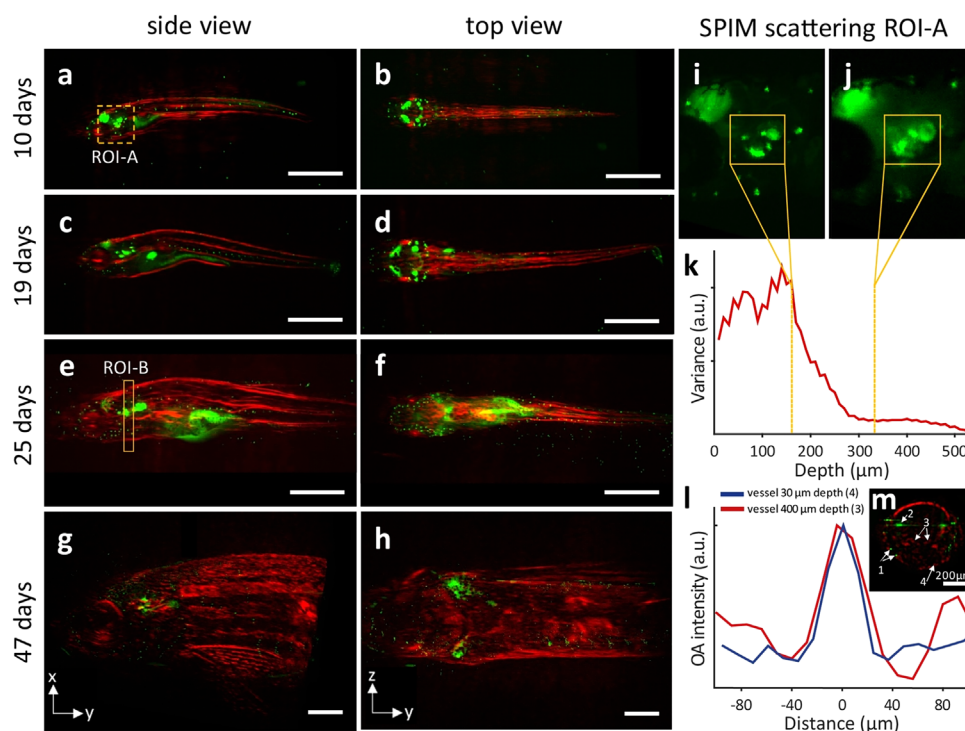
Although not only scattering but also the object itself varies with depth, we focused on scattering variance because the symmetrical anatomy of the zebrafish allows us to compare the same structure at different depths. Therefore, we expected image sharpness of the zebrafish head to be symmetrical around its center at a depth of 260 μm.

Figure 3a–h shows SPIM-optoacoustic mesoscopy imaging of the GFP-expressing zebrafish from the larval stage (10 days) to

adult stage (47 days). While abundant GFP signal with the expected distribution is visible in SPIM images of larvae, the signal is much weaker and less resolved in older animals. In contrast, the red optoacoustic signal from melanin and hemoglobin remains strong at all ages, and overall morphology as well as internal structures are visible. In Figure 3k, a region of interest was chosen and the sharpness was calculated for each image from different depths, and this analysis indicated lower sharpness (increased scattering) with depth. Figure 3i,j compares two images of the same structure on different sides of the head and therefore at different depths. While the structures are expected to be similar due to the symmetry of the head, the images show a different amount of blur due to scattering. The increase in scattering with depth is visible not only in Figure 3k but also by eye.

In contrast, the optoacoustic signal from the vessels identified in the zebrafish remain strong throughout the depth range scanned. As a result, the edges of blood vessels remain sharp even at depths of 400 μm (Figure 3l). The measured full width at half-maximum of the depicted blood vessels was 35 μm in both cases, which is at the resolution limit of the optoacoustic mesoscopy system. These results highlight the complementary nature of the information obtained from SPIM and optoacoustic mesoscopy at a single wavelength.

Next, we focused on the ability of optoacoustic mesoscopy to complement the fluorescence contrast of SPIM. The multi-wavelength capability of optoacoustic mesoscopy allows imaging based on several endogenous sources of contrast, which means that anatomical as well as functional information can be gained noninvasively for early and late developmental stages. Moreover,



**Figure 3.** Hybrid SPIM-optoacoustic mesoscopy imaging of zebrafish development at a single wavelength. Transgenic zebrafish (*Bnn3c:GFP*) expressing GFP in hair cells were imaged at 10, 19, 25, and 47 days after fertilization. GFP fluorescence (green) was imaged using SPIM, while the optoacoustic signal from melanin and hemoglobin (red) was reconstructed using optoacoustic mesoscopy. In both cases, a single excitation wavelength of 488 nm was used. a–h) Side and top views of zebrafish at different developmental stages. A different fish was analyzed at each time point. i, j) Two enlarged views of ROI-A in panel (a), with panel (i) lying at a depth of 160  $\mu\text{m}$  (closer to the objective), and panel (j) lying at a depth of 340  $\mu\text{m}$ . k) Variance of fluorescence intensity as a measure of image sharpness. l) Intensity profile of vessels imaged using optoacoustic mesoscopy, one at a depth of 20–30  $\mu\text{m}$  below the surface [labeled “4” in panel (m)] and the other at a depth of 400  $\mu\text{m}$  [labeled “3” in panel (m)]. m) Cross-sectional view of ROI-B. Cross section taken at rectangle marked on panel (e). Numbers annotate anatomical features: 1, hair cells; 2, ear; 3 and 4, vessels. Scale bars in panels (a–h) indicate 1 mm.

these images can be coregistered perfectly with SPIM images to provide additional, fluorescence-based contrast. These optoacoustic mesoscopy experiments were conducted at two wavelengths to provide contrast due to melanin and hemoglobin. **Figure 4a,b** depicts side and top views, respectively, of zebrafish, while **Figure 4c–e** shows the images obtained after spectrally unmixing the reconstruction data with a linear regression algorithm<sup>[28,29]</sup> to separate the contributions of melanin and hemoglobin. The unmixing revealed several anatomical features, including the hyomandibula, gill filaments, dorsal aorta, and cardinal vein.

To image even more sources of contrast, we expanded the excitation range of our imaging system to the near-infrared region (700–930 nm) and applied a linear multispectral unmixing algorithm using the intrinsic optoacoustic spectra of the sample (**Figure 4f**). The resulting images in **Figure 4g,h** reveal structures different from those observed with wavelengths in the visible region of the spectrum, including blood-containing cardiac structures deep within the fish (**Figure 4g,h**). We attribute the nonblood-containing structures to water and lipid, which absorb more strongly in the near-infrared region. Consistent with this interpretation, **Figure 4j** shows that areas of optoacoustic melanin signal in the upper fin correspond to darkly pigmented areas in a photograph, while areas of putative optoacoustic lipid

and water signal correspond to transparent areas. **Figure 4i** shows the intrinsic spectra for melanin, blood, and lipid structures, which provided the basis for linear unmixing.

Having demonstrated the ability of optoacoustic mesoscopy to complement the range of contrasts that can be imaged in juvenile and adult zebrafish, we wanted to examine whether optoacoustic mesoscopy could detect the same fluorophores as SPIM but in older zebrafish that cannot be imaged well with SPIM. To maximize the signal-to-noise ratio (SNR), we replaced the linear transducer array that we used for the abovementioned studies, which has small transducer elements of  $0.07 \times 3 \text{ mm}^2$ , with a large, spherically focused, single-element detector with a diameter of 10 mm. Tests with 50  $\mu\text{m}$  polystyrene beads embedded in an agar phantom indicated that this change in transducer increased SNR by  $\approx 25 \text{ dB}$ . To allow scanning of the sample over the full  $360^\circ$ , in contrast to the limited angular range of previous optoacoustic mesoscopy set-ups,<sup>[19]</sup> we designed a sample holder that can be spirally rotated and translated in front of a stationary detector (**Figure 5a**). A 45-day-old zebrafish (*cldnb:GFP, sqET4:GFP*) expressing GFP in the hair cells and the lateral line was imaged at 488 and 550 nm (**Figure 5b**). The differential optoacoustic image in **Figure 5e** was obtained by subtracting signals at 550 nm from signals at 488 nm, and it clearly reveals GFP expressed in the brain and lateral line in three dimensions throughout the

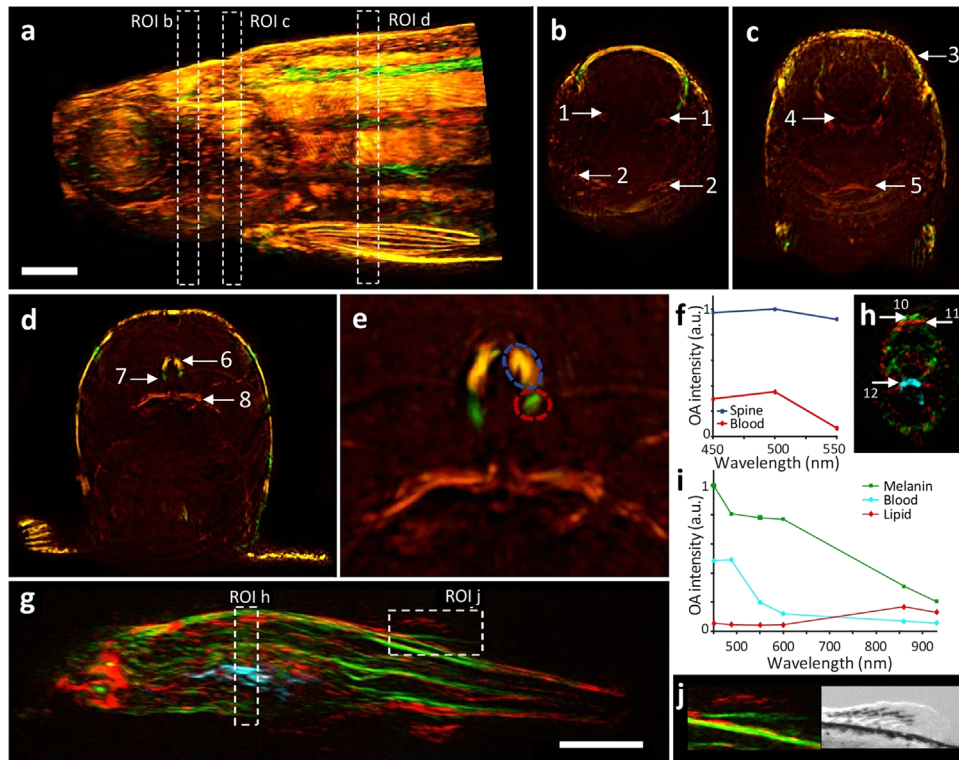


**Figure 4.** Optoacoustic mesoscopy of zebrafish at multiple wavelengths. a–e) A wild-type zebrafish not expressing GFP was imaged at 2 months old after illumination at 450 nm (green) and 550 nm (red). Reconstructions at each of these wavelengths were superimposed, such that overlapping features appear yellow. a) Sideview maximum intensity projection (MIP). b–d) MIPs showing the three ROIs from panel (a). Numbers annotate anatomical features: 1, hyomandibula; 2, gill filaments; 3, semicircular canal; 4, medulla oblongata; 5, cardiac ventricle; 6, spinal cord; 7, cardinal vein; 8, swim bladder. e) Enlarged view of the region in panel (d) around the spine. f) Three-wavelength spectra of the spine and blood marked in panel (e). g–j) A transgenic zebrafish (*Bmn3c:GFP*) at 25 days old was imaged after illumination at 450, 488, 550, 600, 860, and 930 nm. Acoustic data were linearly unmixed and reconstructed such that melanin contrast appears green; lipids, red; and blood vessels, blue. g) Sideview MIP. h) Cross-sectional MIP showing the melanin pigmented skin (10), subcutaneous lipid (11) and blood in the region of the heart (12). i) Unmixed spectra of melanin, blood and lipid. j) Enlarged view of the upper fin from panel (g). Inset, a photograph of the same area. Scale bars in panels (a) and (g) indicate 1 mm.

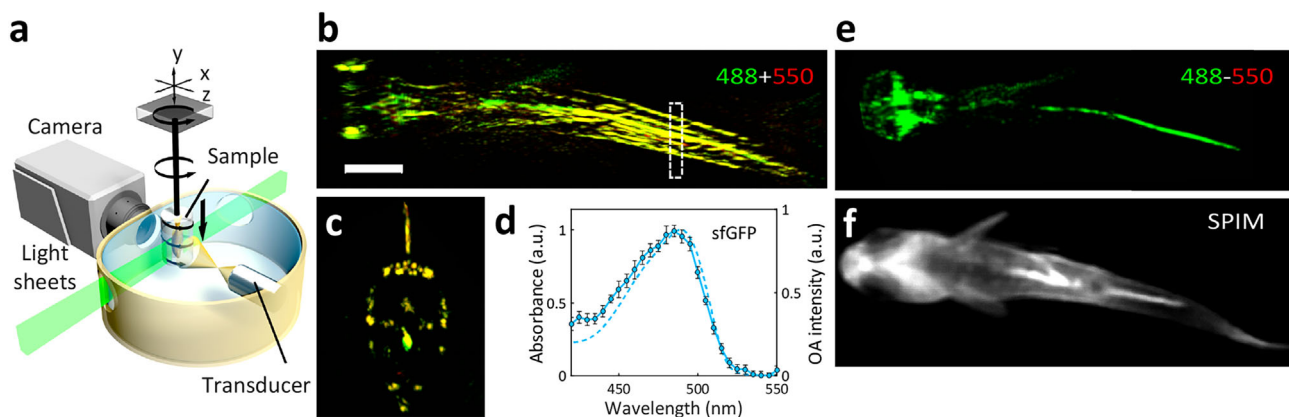


**Figure 5.** Spiral multispectral optoacoustic mesoscopy (SpiMSOM). a) Enlarged view of the adapted sample chamber for the single-element transducer. During the optoacoustic mesoscopy acquisition, the sample is rotated  $360^\circ$  and vertically translated downward. Due to the broad numerical aperture of the transducer, the detector is able to acquire ultrasound signals from the complete sample width without any translation. b) Maximum intensity projections (MIP) of the top view of the superimposed optoacoustic reconstructions at 488 nm (green) and 550 nm (red) of a 45-day-old transgenic zebrafish (*cldnb:GFP*, *SqET4:GFP*). c) Cross-sectional MIP of a region below the fin. d) Normalized absorbance (dotted line) and optoacoustic extinction spectrum (solid line) of superfolder-GFP (see the Experimental Section for details). e) Difference image (488–550 nm) of the optoacoustic reconstructions superimposed in panel (b). f) Average intensity projection of the SPIM image stack of the same fish.

sample. In contrast, Figure 5f shows the average intensity projection of the acquired SPIM image stack for the same fish, revealing the comparatively diffuse GFP signal that overlaps with the signals observed by optoacoustic mesoscopy but with less resolution because SPIM is sensitive to scattered light. These results demonstrate that with an appropriately sensitive detector, optoacoustic mesoscopy can volumetrically image the contrast of genetically encoded fluorescent proteins in living model organisms with good resolution at developmental stages when SPIM functions poorly. Figure 5c depicts the cross-section of the optoacoustic reconstruction marked in Figure 5b, showcasing the depth-imaging abilities of the adapted system. Figure 5d shows the absorption and optoacoustic spectra of GFP, which explain the strong difference in optoacoustic signal generation between 488 and 550 nm.

### 3. Discussion

Here, we describe a novel SPIM-optoacoustic mesoscopy imaging system that significantly improves on the imaging depths that can be achieved with conventional fluorescence microscopy. Whereas previous optoacoustic mesoscopy systems only achieved resolutions sufficient to image adult zebrafish, our hybrid SPIM and optoacoustic tomography system allows the study of zebrafish at every stage of biological development from larvae to adulthood by adding volumetric fluorescence imaging. As we demonstrate here, the hybrid system can detect fluorescence contrast through SPIM and optoacoustic contrast of melanin, blood, lipids, fluorescent proteins, and water. This allows multiscale morphological and functional imaging throughout the zebrafish lifespan, positioning the hybrid system as a useful next-generation tool for developmental, cancer, and neurobiological studies spanning all the life stages.

Among the hallmarks of cancer<sup>[30,31]</sup> are angiogenesis, metastasis, and metabolic reprogramming, and all these processes can be examined with optoacoustics.<sup>[27]</sup> One of the drivers of many cancer hallmarks is hypoxia within tumors, and optoacoustics can measure intratumor oxygenation with high spatiotemporal resolution,<sup>[32]</sup> even in response to perturbations.<sup>[33]</sup> Focal hypoxia in solid tumors may help drive tumor progression and therapy resistance,<sup>[34]</sup> so quantitating hypoxia with our hybrid system may allow in vivo screening of emerging anticancer therapies aimed at inhibiting tumor angiogenesis.<sup>[35]</sup> Indeed, our system might be well suited to exploring how hypoxia can drive angiogenesis and subsequently metastasis.<sup>[36]</sup> Our system is well-positioned to exploit transgenic and genome-modifying tools such as CRISPR/Cas,<sup>[37]</sup> for precise analysis of genes and proteins in healthy and diseased fish from embryonic stages through adulthood. Optoacoustics can also track rapid processes through detection of transgenically expressed reporter proteins, such as the calcium reporter GCaMP.<sup>[38,39]</sup>

Here, we develop an optoacoustic mesoscopy system in which the sample is rotated while the detector remains stationary. This provides better resolution and overall image quality than the previous optoacoustic mesoscopy system,<sup>[19]</sup> and allows deeper imaging within samples than a previous hybrid SPIM-optoacoustic system.<sup>[40]</sup> Our study is the first report of optoacoustic mesoscopy to examine zebrafish morphogenesis at different stages of development. In contrast to previous studies<sup>[24,41]</sup>

that only demonstrated 2D optoacoustic imaging of adult zebrafish without any multispectral unmixing of melanin, blood, and lipids, our system allows for the spectral unmixing of these endogenous absorbers thanks to the broad wavelength range of our laser (420–1000 nm). The ability to image lipids in zebrafish with optoacoustics, by exploiting their near-infrared absorbance peak at 930 nm,<sup>[25]</sup> could lead to a wide range of novel discoveries and insights into lipid-related diseases, including obesity, diabetes, or atherosclerotic plaques.<sup>[42]</sup> More generally imaging in the near infrared offers interesting potential for monitoring developmental changes, e.g., in angiogenesis,<sup>[43]</sup> tissue regeneration,<sup>[44]</sup> cancer studies in zebrafish.<sup>[3]</sup> We also demonstrate with our hybrid system that optoacoustic mesoscopy can detect fluorescent proteins such as GFP, even deep within older zebrafish. Hence, this modality may be compatible with the myriad fluorescent proteins and transgenic expression systems that have been developed for optical microscopy studies,<sup>[45]</sup> which is limited to earlier developmental stages when the organisms remain transparent and thin. Furthermore, our set-up may allow these tools to be extended to in vivo studies of adult stages. At the same time, the range of agents compatible with optoacoustic mesoscopy continues to grow,<sup>[46–48]</sup> opening up additional possibilities for in vivo imaging using our set-up. Drawbacks of the hybrid system include the relatively long acquisition time, motion artifacts during in vivo measurements and potential photobleaching during the scan.

Our novel hybrid system allows imaging of fluorescence and optoacoustic signal to visualize components and processes at the tissue and organismal levels. In addition, the multispectral capability of the system allows the distribution of numerous target molecules or tissues to be imaged simultaneously, either in a label-free way or following expression or injection of exogenous contrast agents. Our set-up is compatible with other model organisms such as *Xenopus* and axolotls, and it may be particularly useful for organisms that go from transparent to opaque during development and so cannot be analyzed at later developmental stages in vivo using conventional optical microscopy.

### 4. Experimental Section

**Experimental Set-Up:** To provide the light sheet illumination for SPIM and homogenous illumination for optoacoustic imaging, a fast tunable nanosecond-laser was used (7 ns, 19 mJ) at 450 nm, tunable from 420 to 700 nm, Spitlight-DPSS 250 ZHG-OPO, Innolas, Germany). The laser beam was aligned to the illumination paths for SPIM and optoacoustic mesoscopy (Figure 1). A half-wave plate (HWP) and a polarizing beam splitter (PBS) were used to reduce the power to 25% for SPIM illumination. The light sheet for SPIM imaging was obtained using a cylindrical lens (CL) and an adjustable aperture (A), and consequently rotated by 90° using a dove prism (DP). The light sheet was divided at a second PBS to obtain double-sided illumination. With a flip mirror (FM) behind the first PBS, the beam was reflected to create a squared, homogeneous beam profile for optoacoustic imaging. Volumetric illumination was achieved by focusing the laser pulse on a diffuser (D), which was placed in front of a light mixing rod (LMR). The lens pairs L2L3 and L2L4 enlarged the squared beam profile to 10×10 mm<sup>2</sup> in the sample chamber, which was again divided by the PBS for double-sided illumination. The maximum energy per pulse reaching the sample was measured as 3.5 mJ for both illumination paths.

**Hybrid SPIM and Optoacoustic Mesoscopy:** To examine the combination of SPIM and optoacoustic mesoscopy for visualizing zebrafish development, *Bnn3c:GFP* zebrafish were used. Fish from the same clutch were

imaged at different ages and stages of development; this imaging was conducted *ex vivo* because the fish were older than 5 days, as stipulated in local ethics regulations. Fish were immersed in paraformaldehyde (PFA) for 0.5–3 h based on size. This preserved the fish from decay, while negligibly affecting optoacoustic signal strength. Fish were embedded in a cylinder of agarose. Although imaging was performed *ex vivo*, both SPIM and OA are also suitable for *in vivo* imaging of agarose-embedded zebrafish.<sup>[9]</sup> SPIM was used to collect fluorescence signal from the GFP within the zebrafish at an excitation wavelength of 488 nm, while single-wavelength optoacoustic mesoscopy was used to detect the optoacoustic signal from melanin. Fish were scanned through the perpendicular light sheet on a translational stage (M-112.1DG; PI Micro, Germany). Fluorescence acquisition was performed with a scientific complementary metal oxide semiconductor (sCMOS) camera (pco.edge, PCO, Germany). Subsequently, the sample was rotated by 90°, then scanned again for multiview acquisition. Using fluorescent beads, the minimal axial SPIM resolution was determined to be  $\approx 35 \mu\text{m}$ . The lateral resolution in the *xy*-plane, determined by the optical zoom and the camera, was  $6.15 \mu\text{m}$ .

Ultrasound detection of the samples in Figures 3 and 4 was performed using a cylindrically focused, wide-bandwidth ultrasonic transducer array (24 MHz center frequency, 55% bandwidth at  $-6 \text{ dB}$ , 128 elements, Vermon, France). The translation-rotation scanning geometry was based on the concept presented by Gateau et al.<sup>[18]</sup> In contrast to the system described by Gateau et al.,<sup>[18]</sup> here the sample was rotated over 360° using a rotational stage (RS-40, PI Micro, Germany) and the ultrasound linear array was translated at each angular position with a linear stage (M-111.1DG, PI Micro, Germany), which reduces heterogeneity in image quality due to limited-view detection. The detector was typically translated at a total number of 90 angular positions. The sample was positioned using three linear stages in the *x*-, *y*-, and *z*-directions (M-112.1DG, M-403.2DG, and M-112.1DG, PI Micro, Germany). The system included an additional rotational stage (M-061.PD, PI Micro, Germany) for rotating the array, which allowed the detector to be moved so that the system was able to exploit the whole scanning range while running in SPIM mode. The acquisition time for one optoacoustic scan using the linear array was typically about 30 min per wavelength.

To increase sensitivity for the optoacoustic imaging experiment in Figure 5, the linear array was replaced with a spherically focused, single-element ultrasonic transducer (20 MHz center frequency, 77% bandwidth at  $-6 \text{ dB}$ , Imasonic, France). In the novel spiral scanning geometry with the single-element detector, the sample is rotated continuously at the maximum speed of the rotation stage, while being slowly and simultaneously translated in the *y*-direction. The high numerical aperture of the detector enables detection of ultrasonic signals across the lateral width of the sample without any translation of the detector. The acquisition time for one optoacoustic scan using a single-element was typically about 60 min for four wavelengths simultaneously. This relatively fast imaging time was possible because the sample was moving continuously and every single emitted laser pulse provided by the OPO was used. In the future, the imaging speed could be significantly increased by using a faster rotation stage.

Following the optoacoustic scan, the raw signals were filtered using a third-order Butterworth filter, then reconstructed using a weighted back-projection algorithm.<sup>[18,49]</sup> For data used for linear unmixing, a Hilbert transform was applied to the data before the reconstruction in order to remove negative values caused by the thermal expansion and contraction of the object<sup>[50]</sup> and improve data quality for unmixing.<sup>[18]</sup> The weighted back-projection was performed on cuboid voxels with a size of  $12 \times 12 \times 35 \mu\text{m}^3$  for array scans and  $8 \times 8 \times 16 \mu\text{m}^3$  for single-element scans, which exhibited a lower number of projections. The 3D image stacks were obtained using maximum intensity projections (MIP) and visualized with Amira (Amira 6.2, Thermo Fisher Scientific, USA). Characterization with polymer beads of 10–20  $\mu\text{m}$  revealed a resolution of  $35 \times 35 \times 120 \mu\text{m}$  in the *x*-, *y*-, and *z*-directions for the array and  $35 \times 35 \times 100 \mu\text{m}$  for the single-element detector. These values are consistent with the specifications of the transducers.

**Multispectral Optoacoustic Mesoscopy (MSOM):** To examine the ability of the hybrid SPIM-optoacoustic mesoscopy system to provide optoacoustic information simultaneously from multiple components of tissue, wild-

type adult zebrafish was imaged (2 months old, ZDB-GENO-960809-7) *ex vivo* using optoacoustic mesoscopy as described above, except that the animals using light at 430, 450, 488, and 550 nm were illuminated to stimulate the different optoacoustic spectra of hemoglobin and melanin. The raw optoacoustic data were spectrally unmixed using a linear regression method as described by Razansky et al.<sup>[28]</sup> Extinction spectra of melanin and blood were extracted from the reconstruction volume's intensity profiles in regions corresponding to the four wavelengths measured. When visualizing fluorescent proteins such as GFP, image reconstructions were overlaid at 488 and 550 nm (Figure 5b) and subtracted the two reconstructions (488–500 nm; Figure 5e). The optoacoustic spectrum shown in Figure 5d was measured with the same laser but a different system as described elsewhere.<sup>[51]</sup>

**Reconstruction:** Fluorescence images acquired by SPIM were processed using a space-variant blind deconvolution algorithm<sup>[52]</sup> and optoacoustic images were reconstructed using a 3D backprojection algorithm. Both datasets were then fused in Amira (Amira 6.2, Thermo Fisher Scientific, USA). The relative positions of the SPIM and OA reconstruction volumes were determined based on the geometric parameters of the system and after manual adjustment to maximize overlap of the microspheres visible in both modalities.

## Acknowledgements

P.V. and B.K.-S. contributed equally to this work. The authors wish to thank A. Chmyrov, A. C. Rodríguez, R. J. Wilson, and S. M.L Lee for discussions on the manuscript. The authors thank L. Pola-Morell (Research Unit Sensory Biology and Organogenesis, Helmholtz Zentrum München, Neuherberg, Germany) for kindly providing mutant and wild-type zebrafish. The research leading to these results has received funding by the Bundesministerium für Bildung und Forschung (BMBF), Bonn, Germany (Project Nos. Tech2See, 13N12623, and 13N12624). All authors declare that they have no competing interests.

Open access funding enabled and organized by Projekt DEAL.

## Conflict of Interest

The authors declare no conflict of interest.

## Data Availability Statement

Data is available from the corresponding author upon reasonable request.

## Keywords

fluorescence microscopy, selective plane illumination microscopy, multispectral optoacoustic tomography, photoacoustic imaging, zebrafish development

Received: November 8, 2022

Revised: April 21, 2023

Published online: June 3, 2023

- [1] D. M. Langenau, L. I. Zon, *Nat. Rev. Immunol.* **2005**, *5*, 307.
- [2] R. White, K. Rose, L. Zon, *Nat. Rev. Cancer* **2013**, *13*, 624.
- [3] R. Fior, V. Póvoa, R. V. Mendes, T. Carvalho, A. Gomes, N. Figueiredo, M. G. Ferreira, *Proc. Natl. Acad. Sci. USA* **2017**, *114*, E8234.
- [4] C. A. Macrae, R. T. Peterson, *Nat. Rev. Drug Discovery* **2015**, *14*, 721.
- [5] M. Kleinert, C. Clemmensen, S. M. Hofmann, M. C. Moore, S. Renner, S. C. Woods, P. Huypens, J. Beckers, M. H. De Angelis, A. Schürmann, M. Bakhti, M. Klingenspor, M. Heiman, A. D. Cherrington, M. Ristow, H. Lickert, E. Wolf, P. J. Havel, T. D. Müller, M. H. Tschöp, *Nat. Rev. Endocrinol.* **2018**, *14*, 140.

- [6] H. Feitsma, E. Cuppen, *Mol. Cancer Res.* **2008**, *6*, 685.
- [7] V. Ntziachristos, *Nat. Methods* **2010**, *7*, 603.
- [8] J. Huisken, D. Y. R. Stainier, *Development* **2009**, *136*, 1963.
- [9] M. Mickoleit, B. Schmid, M. Weber, F. O. Fahrbach, S. Hombach, S. Reischauer, J. Huisken, *Nat. Methods* **2014**, *11*, 919.
- [10] M.-T. Ke, S. Fujimoto, T. Imai, *Nat. Neurosci.* **2013**, *16*, 1154.
- [11] R. M. White, A. Sessa, C. Burke, T. Bowman, J. Leblanc, C. Ceol, C. Bourque, M. Dovey, W. Goessling, C. E. Burns, L. I. Zon, *Cell Stem Cell* **2008**, *2*, 183.
- [12] M. Omar, J. Gateau, V. Ntziachristos, *Opt. Lett.* **2013**, *38*, 2472.
- [13] M. Omar, J. Rebling, K. Wicker, T. Schmitt-Manderbach, M. Schwarz, J. Gateau, H. López-Schier, T. Mappes, V. Ntziachristos, *Light: Sci. Appl.* **2017**, *6*, e16186.
- [14] J. Aguirre, M. Schwarz, N. Garzorz, M. Omar, A. Buehler, K. Eyerich, V. Ntziachristos, *Nat. Biomed. Eng.* **2017**, *1*, 0068.
- [15] M. Omar, D. Soliman, J. Gateau, V. Ntziachristos, *Opt. Lett.* **2014**, *39*, 3911.
- [16] M. Omar, M. Schwarz, D. Soliman, P. Symvoulidis, V. Ntziachristos, *Neoplasia* **2015**, *17*, 208.
- [17] M. Schwarz, A. Buehler, J. Aguirre, V. Ntziachristos, *J Biophotonics* **2016**, *9*, 55.
- [18] J. Gateau, M. Á. A. Caballero, A. Dima, V. Ntziachristos, *Med. Phys.* **2013**, *40*, 0133021.
- [19] J. Gateau, A. Chekkoury, V. Ntziachristos, *Opt. Lett.* **2013**, *38*, 4671.
- [20] A. Chekkoury, A. Nunes, J. Gateau, P. Symvoulidis, A. Feuchtinger, N. Beziere, S. V. Ovsepian, A. Walch, V. Ntziachristos, *Neoplasia* **2016**, *18*, 459.
- [21] D. Razansky, C. Vinegoni, V. Ntziachristos, *Phys. Med. Biol.* **2009**, *54*, 2769.
- [22] Na Huang, H. Guo, W. Qi, Z. Zhang, J. Rong, Z. Yuan, W. Ge, H. Jiang, L. Xi, *Biomed. Opt. Express* **2016**, *7*, 3543.
- [23] Q. Chen, T. Jin, W. Qi, X. Mo, L. Xi, *Biomed. Opt. Express* **2017**, *8*, 2359.
- [24] M. Liu, N. Schmitner, M. G. Sandrian, B. Zabihian, B. Hermann, W. Salvenmoser, D. Meyer, W. Drexler, *Biomed. Opt. Express* **2013**, *4*, 1846.
- [25] P. Beard, *Interface Focus* **2011**, *1*, 602.
- [26] J. Weber, P. C. Beard, S. E. Bohndiek, *Nat. Methods* **2016**, *13*, 639.
- [27] X. L. Deán-Ben, S. Gottschalk, B. Mc Larney, S. Shoham, D. Razansky, *Chem. Soc. Rev.* **2017**, *46*, 2158.
- [28] D. Razansky, M. Distel, C. Vinegoni, R. Ma, N. Perrimon, R. W. Köster, V. Ntziachristos, *Nat. Photonics* **2009**, *3*, 412.
- [29] S. Tzoumas, N. Deliolaris, S. Morscher, V. Ntziachristos, *IEEE Trans. Med. Imaging* **2014**, *33*, 48.
- [30] D. Hanahan, R. A. Weinberg, *Cell* **2000**, *100*, 57.
- [31] D. Hanahan, R. A. Weinberg, *Cell* **2011**, *144*, 646.
- [32] V. Ermolayev, X. L. Dean-Ben, S. Mandal, V. Ntziachristos, D. Razansky, *Eur. Radiol.* **2016**, *26*, 1843.
- [33] M. R. Tomaszewski, I. Q. Gonzalez, J. P. O'connor, O. Abeyakoon, G. Jm Parker, K. J. Williams, F. J. Gilbert, S. E. Bohndiek, *Theranostics* **2017**, *7*, 2900.
- [34] J. D. Martin, D. Fukumura, D. G. Duda, Y. Boucher, R. K. Jain, *Cold Spring Harb. Perspect Med.* **2016**, *6*, a027094.
- [35] A. Albini, F. Tosetti, V. W. Li, D. M. Noonan, W. W. Li, *Nat. Rev. Clin. Oncol.* **2012**, *9*, 498.
- [36] S. L. C. Lee, P. Rouhi, L. D. Jensen, D. Zhang, H. Ji, G. Hauptmann, P. Ingham, Y. Cao, *Proc. Natl. Acad. Sci. USA* **2009**, *106*, 19485.
- [37] W. Y. Hwang, Y. Fu, D. Reyon, M. L. Maeder, S. Q. Tsai, J. D. Sander, R. T. Peterson, J.-R. J. Yeh, J. K. Joung, *Nat. Biotechnol.* **2013**, *31*, 227.
- [38] X. L. Deán-Ben, G. Sela, A. Lauri, M. Kneipp, V. Ntziachristos, G. G. Westmeyer, S. Shoham, D. Razansky, *Light: Sci. Appl.* **2016**, *5*, e16201.
- [39] X. L. Deán-Ben, S. Gottschalk, G. Sela, S. Shoham, D. Razansky, *Opt. Lett.* **2017**, *42*, 959.
- [40] H.-C. A. Lin, A. Chekkoury, M. Omar, T. Schmitt-Manderbach, B. Koberstein-Schwarz, T. Mappes, H. López-Schier, D. Razansky, V. Ntziachristos, *Laser Photonics Rev.* **2015**, *9*, L29.
- [41] R. Ma, M. Distel, X. L. Deán-Ben, V. Ntziachristos, D. Razansky, *Phys. Med. Biol.* **2012**, *57*, 7227.
- [42] M. Hölttä-Vuori, V. T. V. Salo, L. Nyberg, C. Brackmann, A. Enejder, P. Panula, E. Ikonen, *Biochem. J.* **2010**, *429*, 235.
- [43] G. N. Serbedzija, *Angiogenesis* **1999**, *3*, 353.
- [44] C. Jopling, E. Sleep, M. Raya, M. Martí, A. Raya, J. C. I. Belmonte, *Nature* **2010**, *464*, 606.
- [45] N. C. Shaner, P. A. Steinbach, R. Y. Tsien, *Nat. Methods* **2005**, *2*, 905.
- [46] A. P. Jathoul, J. Laufer, O. Ogunlade, B. Treeby, B. Cox, E. Zhang, P. Johnson, A. R. Pizzey, B. Philip, T. Marafioti, M. F. Lythgoe, R. B. Pedley, M. A. Pule, P. Beard, *Nat. Photonics* **2015**, *9*, 239.
- [47] J. Stritzker, L. Kirscher, M. Scadeng, N. C. Deliolaris, S. Morscher, P. Symvoulidis, K. Schaefer, Q. Zhang, L. Buckel, M. Hess, U. Donat, W. G. Bradley, V. Ntziachristos, A. A. Szalay, *Proc. Natl. Acad. Sci. USA* **2013**, *110*, 3316.
- [48] A. Mishra, G. Pariani, T. Oerther, M. Schwaiger, G. G. Westmeyer, *Anal. Chem.* **2016**, *88*, 10790.
- [49] M. Xu, L. V. Wang, *Phys. Rev. E* **2005**, *71*, 016706.
- [50] G. J. Diebold, T. Sun, M. I. Khan, *Phys. Rev. Lett.* **1991**, *67*, 3384.
- [51] P. Vetschera, K. Mishra, J. P. Fuenzalida-Werner, A. Chmyrov, V. Ntziachristos, A. C. Stiel, *Anal. Chem.* **2018**, *90*, 10527.
- [52] K.-S. Benno, O. Lars, S.-M. Tobias, M. Timo, N. Vasilis, *J. Biomed. Opt.* **2016**, *21*, 096005.